

What’s the slope of galaxy clusters intrinsic alignment?

Davide Piras¹★ and Benjamin Joachimi²

¹*Dipartimento di Fisica “G. Galilei”, Università di Padova, via Marzolo 8, I-35131 Padova, Italy*

²*Department of Physics and Astronomy, University College London, Gower Street, London WC1E 6BT, UK*

8 April 2017

ABSTRACT

This is a simple template for authors to write new MNRAS papers. The abstract should briefly describe the aims, methods, and main results of the paper. It should be a single paragraph not more than 250 words (200 words for Letters). No references should appear in the abstract.

Key words: intrinsic alignment – Millennium simulation – Millennium-XXL simulation

1 INTRODUCTION

TALK ABOUT INTRINSIC ALIGNMENT, AND WHY IT IS IMPORTANT (FUTURE SURVEYS) When looking at the sky, one would expect to see randomly distributed stars and galaxies, assuming a homogeneous and isotropic universe, whereas correlation between galaxies orientation is actually observed; plenty of reasons can be exhibited to explain this, as . Moreover, intrinsic alignment In this work we show an analysis for both galaxies and galaxy clusters using simulation (Sect. 2) and real data (Sect. 4); our method is presented in Sect. 3.

2 DATA

In this work we consider haloes from two different simulations:

(i) the **Millennium Simulation (MS)**, first presented in [Springel et al. \(2005\)](#), which uses 2160^3 dark matter particles of mass $m_P = 1.2 \times 10^9 M_\odot$ enclosed in a 500-Mpc/ h -side box to sample dark matter haloes and study their growth. In particular, we take into consideration 2 of its 64 snapshots, i.e. the one at $z = 0$ (snapshot 63), which we use for all our analysis, and the one at $z \simeq 0.45$ (snapshot 49), which is studied only as an aside.

*** I AM NOT SURE ABOUT THIS PART BECAUSE WE NEVER DISCUSSED ABOUT IT: HOW WAS OUR CATALOGUE BUILT?*** Dark matter haloes are identified as in [Joachimi et al. \(2013a\)](#) and references therein; the shape of each halo is described by the eigenvalues and eigenvectors of the simple inertia tensor

$$\mathbf{M}_{\mu\nu} = m_P \sum_{i=1}^{N_P} r_{i,\mu} r_{i,\nu} \quad (1)$$

where N_P is the total number of particles within the halo, and \mathbf{r}_i is the vector that indicates the position of the i -th particle with respect

to the centre of the halo, i.e. the gravitational potential minimum. In Fig. 2 we also show the results that we obtain if we consider a reduced inertia tensor, which is defined as ([Pereira et al. 2008](#)):

$$\mathbf{M}_{\mu\nu}^{red} = m_P \sum_{i=1}^{N_P} \frac{r_{i,\mu} r_{i,\nu}}{r_i^2} \quad (2)$$

with r_i^2 the square of the three-dimensional distance of the i -th particle from the centre of the halo; the reduced inertia tensor is more weighted towards the centre of the halo, and may yield a more reliable approximation of the shape of the galaxy ([Joachimi et al. 2013b](#); [Chisari et al. 2015](#)). We place the eigenvector corresponding to the largest eigenvalue along the line of sight, and project the ellipsoid onto the plane of the sky defined by this choice: the resulting ellipse is the shape of the galaxy. We proceed as in [Joachimi et al. \(2013a\)](#) to define the ellipticity of the galaxy, considering our objects as early-type galaxies: indicating the three unit eigenvectors as $\mathbf{s}_\mu = \{s_{x,\mu}, s_{y,\mu}, s_{||,\mu}\}^\top$ and the absolute values of the semi-axes as ω_μ , $\mu \in \{1, 2, 3\}$, we define a symmetric tensor

$$\mathbf{W}^{-1} = \sum_{\mu=1}^3 \frac{s_{\perp,\mu} s_{\perp,\mu}^\top}{\omega_\mu^2} - \frac{\kappa \kappa^\top}{\alpha^2} \quad (3)$$

with $s_{\perp,\mu} = \{s_{x,\mu}, s_{y,\mu}\}^\top$ the eigenvector projected along the line of sight,

$$\kappa = \sum_{\mu=1}^3 \frac{s_{||,\mu} \mathbf{s}_{\perp,\mu}}{\omega_\mu^2} \quad (4)$$

and

$$\alpha^2 = \sum_{\mu=1}^3 \left(\frac{s_{||,\mu}}{\omega_\mu} \right)^2. \quad (5)$$

We then compute the two components of the complex polarisation e , which defines the galaxy ellipticity ([Bartelmann & Schneider](#)

★ E-mail: davide.piras@studenti.unipd.it

2001):

$$e_1 = \frac{W_{11} - W_{22}}{W_{11} + W_{22}}; \quad (6)$$

$$e_2 = \frac{2W_{12}}{W_{11} + W_{22}}. \quad (7)$$

(ii) the **Millennium-XXL Simulation (MXXLS)**, which samples 6720^3 dark matter particles of mass $m_P = 8.456 \times 10^9 M_\odot$ confined in a cubic region of $3000 \text{ Mpc}/h$ on a side (Angulo et al. 2012); in this case, we consider only one snapshot, at $z = 0$. Particles are selected using an ellipsoidal overdensity algorithm, as described in Despali et al. (2013) and in Bonamigo et al. (2015); the shape of the haloes is then derived as for the MS from the eigenvectors and eigenvalues of the mass tensor

$$\mathbf{M}_{\mu\nu} = m_P \sum_{i=1}^{N_P} \frac{r_{i,\mu} r_{i,\nu}}{M_{TOT}} = \frac{1}{N_P} \sum_{i=1}^{N_P} r_{i,\mu} r_{i,\nu} \quad (8)$$

with M_{TOT} the total mass of the object. Note that the mass tensor (Eq. 8) and the inertia tensor (Eq. 1) are different quantities (Bett et al. 2007), but the analysis on the two simulations yields pretty consistent results, as will be shown; also, for this catalogue no “reduced” tensor is taken into consideration.

In the simulations the same set of cosmological parameters is adopted, namely they both assume a spatially flat Λ CDM universe with the total matter density $\Omega_m = \Omega_b + \Omega_{dm} = 0.25$, where $\Omega_b = 0.045$ indicates baryons and $\Omega_{dm} = 0.205$ represents dark matter, a cosmological constant $\Omega_\Lambda = 1 - \Omega_m = 0.75$, the Hubble parameter $h = 0.73$ and the density variance in spheres of radius $8 \text{ Mpc}/h$ $\sigma_8 = 0.9$. All the density parameters are in units of the critical density.

3 METHODOLOGY

To measure the correlation between the shapes of galaxy clusters and the density field we proceed as in van Uitert & Joachimi (2017), namely we define an estimator as a function of the comoving transverse distance R_p and the line-of-sight distance Π :

$$\hat{\xi}_{g+}(R_p, \Pi) = \frac{S_+ D_d}{D_s D_d} - \frac{S_+ R}{D_s R}, \quad (9)$$

where $S_+ D_d$ represents the correlation between cluster shapes and the density sample, $D_s D_d$ the number of cluster shape - density pairs, $S_+ R$ the correlation between cluster shapes and random points and $D_s R$ the number of cluster shape - random point pairs. We then integrate along the line of sight to obtain the total projected intrinsic alignment signal:

$$\hat{w}_{g+}(R_p) = \int_0^{\Pi_{max}} d\Pi \hat{\xi}_{g+}(R_p, \Pi); \quad (10)$$

throughout this work, we adopt $\Pi_{max} = 60 \text{ Mpc}/h$, a value large enough not to miss part of the signal but small enough not to pick up too much noise. ***ASK IF $\Pi_{min} = 0$ IS CORRECT***

We describe the intrinsic alignment signal by simplifying the model in van Uitert & Joachimi (2017), namely we assume:

$$w_{g+}(R_p, M) = A_{IA}(M) b_g(M) w_{\delta+}^{model}(R_p), \quad (11)$$

with $A_{IA}(M)$ the amplitude of the intrinsic alignment signal, $b_g(M)$ the cluster bias and $w_{\delta+}^{model}(R_p)$ a function in which we include the dependence on R_p (van Uitert & Joachimi 2017, equation 5); the

dependence in the mass of the halo M is in both the $A_{IA}(M)$ and $b_g(M)$ factors.

We also use the LS (Landy & Szalay 1993) estimator to calculate the clustering signal:

$$\hat{\xi}_{gg}(R_p, \Pi) = \frac{D_d D_d - 2D_d R + RR}{RR}, \quad (12)$$

where $D_d D_d$ represents the number of cluster pairs, $D_d R$ the number of cluster - random point pairs, and RR the number of random point pairs. We then integrate along the line of sight to obtain the total projected clustering signal:

$$\hat{w}_{gg}(R_p) = \int_0^{\Pi_{max}} d\Pi \hat{\xi}_{gg}(R_p, \Pi). \quad (13)$$

We describe the clustering signal with a simple model:

$$w_{gg}(R_p, M) = b_g^2(M) w_{\delta\delta}^{model}(R_p), \quad (14)$$

with $w_{\delta\delta}^{model}(R_p)$ a function in which we include the dependence on R_p (van Uitert & Joachimi 2017, equation 9).

To get rid of the cluster bias $b_g(M)$ factor and focus on the mass dependence of the amplitude $A_{IA}(M)$, we define:

$$r_{g+}(R_p, M) = \frac{w_{g+}(R_p, M)}{\sqrt{w_{gg}(R_p, M)}} = \frac{A_{IA}(M) w_{\delta+}^{model}(R_p)}{\sqrt{w_{\delta\delta}^{model}(R_p)}} \quad (15)$$

where we assume that the clustering signal $w_{gg}(R_p, M)$ is positive, which is indeed true if we evaluate it at a reasonably small $R_p = R_p^*$ - see Sect. 4 and Fig. 1 for further discussion. If we evaluate the whole expression in Eq. 15 at this same value R_p^* , which we adopt to be the midpoint of a logarithmic bin which covers $6 \text{ Mpc}/h < R_p < 30 \text{ Mpc}/h$, we obtain the quantity:

$$r_{g+}(M) = r_{g+}(R_p = R_p^*, M) \propto A_{IA}(M) \quad (16)$$

where we stress that this quantity now only depends on the mass of the halo M . The goal of this paper is to study the dependence on the mass of the amplitude $A_{IA}(M)$ by studying the quantity $r_{g+}(M)$: assuming that

$$A_{IA}(M) \propto M^\beta, \quad (17)$$

we adopt the following model for $r_{g+}(M)$:

$$r_{g+}(M) = A \cdot \left(\frac{M}{M_r} \right)^\beta \quad (18)$$

with A a generic amplitude with no physical meaning, $M_r = 10^{13.5} M_\odot / h_{70}$ a pivot mass and β as in Eq. 17.

To achieve this goal, we select the objects of the catalogues described in Sect. 2 in $n = 5$ logarithmic mass bins, between $10^{11} M_\odot$ and $10^{14} M_\odot$ for the MS and between $10^{12.5} M_\odot$ and $10^{15} M_\odot$ for the MXXLS, we split them in $N = 3^3 = 27$ sub-boxes based on their positions inside the cube of the respective simulation, and calculate w_{g+} and w_{gg} for each of the N sub-samples by replacing the integrals in Eq. 10 and 13 with a sum over 20 line-of-sight bins, each $(\Pi_{max} - \Pi_{min})/20 \text{ Mpc}/h$ wide.

We then perform a posterior analysis over the data to retrieve the distributions of A and β : according to Bayes' theorem, if \mathbf{d} is the vector of the data and \mathbf{p} the vector of the parameters,

$$P(\mathbf{p}|\mathbf{d}) \propto P(\mathbf{d}|\mathbf{p}) P(\mathbf{p}) \propto e^{-\frac{1}{2}\chi^2} P(\mathbf{p}) \quad (19)$$

with $P(\mathbf{p}|\mathbf{d})$ the posterior probability, $P(\mathbf{d}|\mathbf{p})$ the likelihood function, $P(\mathbf{p})$ the prior probability and $\chi^2 = (\mathbf{d} - \mathbf{m})^T \mathbf{C}^{-1} (\mathbf{d} - \mathbf{m})$, with \mathbf{m} the vector of the model and \mathbf{C}^{-1} the precision matrix, the inverse of the covariance matrix \mathbf{C} . We assume flat, uninformative

priors in the fit with ranges $\log_{10} A \in [-1.7; -0.6]$ and $\beta \in [0; 0.5]$. We estimate the covariance matrix from the data as in Taylor et al. (2013):

$$\mathbf{C}_{\mu\nu} = \frac{1}{N-1} \sum_{i=1}^N (x_{i,\mu} - \bar{x}_\mu)(x_{i,\nu} - \bar{x}_\nu) \quad (20)$$

with $\mu, \nu \in \{1, \dots, n\}$, $\bar{x}_\mu = \frac{1}{N} \sum_{i=1}^N x_{i,\mu}$, and $x_{i,\mu} = r_{g+}(M)$ for each sub-box and each mass bin, as defined in Eq. 16. We then invert the covariance matrix and correct the bias on the inverse to obtain an unbiased estimate of the precision matrix, given by:

$$\mathbf{C}_{\text{unbiased}}^{-1} = \frac{N-n-2}{N-1} \mathbf{C}^{-1} \quad (21)$$

where we assume $N > n+2$. The results of the analysis are presented in Sect. 4.

The choice of n and N is constrained by many factors: first of all, if N is too large the single values of w_{gg} (and w_{g+}) tend to fluctuate around the mean, thus increasing the error bar and sometimes plunging below 0, which is unacceptable for our choice of $r_{g+}(R_p, M)$, as specified after Eq. 15. Furthermore, we want n to be large enough to be capable of displaying the trend of the signals along the whole mass range chosen. Finally, we need to take $n \ll N$ to avoid divergences related to the fact that we estimate the covariance from a finite number of samples (Taylor et al. 2013).

4 RESULTS AND DISCUSSION

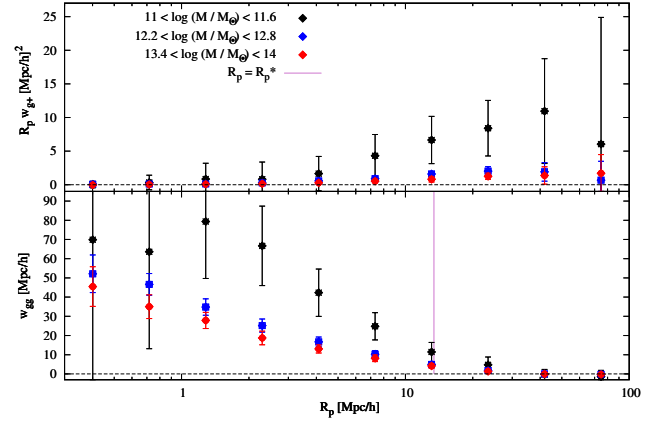
The trend of w_{g+} and w_{gg} with R_p for the lowest, middle and highest mass bin for both the catalogues is shown in Fig. 1; note that around $R_p = R_p^*$ w_{gg} is always positive within the error bar, therefore Eq. 16 always returns a real value. The points showed in Fig. 1 are the arithmetical mean of the N values for each mass bin, while the error bars are represented by the standard deviation of the values. The overall behaviour of w_{g+} and w_{gg} agrees with previous works (Joachimi et al. 2011; van Uitert & Joachimi 2017) and the upper plot in each panel suggests the detection of a positive alignment, meaning that clusters point towards nearby clusters.

We then study the dependence of w_{g+} , w_{gg} and r_{g+} on the mass of the haloes, which we define to be the mass within a sphere centred on the potential minimum which has mean density 200 times the mean value at $z = 0$ (M_{200m}): in this way, we are able to compare our results with those in van Uitert & Joachimi (2017, figure 7).

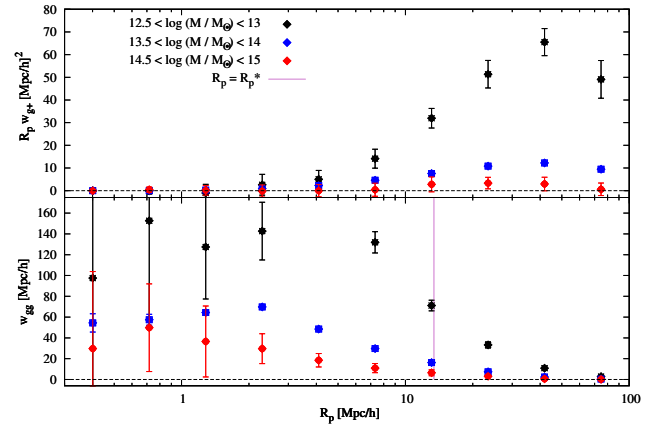
ARE WE SURE THAT THE DEFINITION OF THE VIRIAL MASS IS THE SAME IN BOTH THE SIMULATIONS? CAN'T FIND ANY REFERENCE FOR THE MILLENNIUM, BUT FOR THE MXXLS THEY SAY CONVENTIONAL, SO IT SHOULD BE OK

In Fig. 2 we also include, for the Millennium simulation only, two more results: purple dots represent the signal from the objects at redshift $z = 0.46$, while light blue dots represent the signal from the objects at $z = 0$ but using the reduced inertia tensor (*rit*) instead of the simple one to measure the shapes of the haloes.

*** NOTE THAT THE CONVERSION OF MASS ALSO DEPENDS ON REDSHIFT, SO A DIFFERENT TABLE IS USED FOR PURPLE DOTS *** As one can see, despite the use of different quantities to measure the shapes of the objects, as explained in Sect. 2, the MS and the MXXLS yield consistent results in the mass range where they overlap; furthermore, all three w_{g+} , w_{gg} and r_{g+} increase with increasing mass. As a side note, we mention that



(a) w_{g+} and w_{gg} for the Millennium simulation.



(b) w_{g+} and w_{gg} for the Millennium XXL simulation.

Figure 1. Trend of the intrinsic alignment signal w_{g+} and the cluster signal w_{gg} with the comoving transverse distance R_p for (a) the Millennium and (b) the Millennium XXL simulation. Note that at $R_p = R_p^* = 13.42$ Mpc/h the w_{gg} signal is positive within the error bar. Red, blue and black dots represent respectively the lowest, middle and highest mass bin of each catalogue.

using the *rit* leads to lower alignment signals, as found in ***ADD PREVIOUS WORKS***

*** MAYBE AT SOME POINT WE SHOULD DISCUSS THE IC CORRECTION? ***

We proceed by showing the results of the posterior analysis described in Sect. 3: Fig. 3(a) and Fig. 3(b) display the outcomes of the separated analysis on the two simulations, while Fig. 3(c) shows the results from the joint analysis of the two catalogues, obtained by multiplying the likelihood functions and assuming the same flat priors on the parameters. The most stringent bounds come from the MXXL simulation, while the Millennium yields larger errors on the parameters, even though consistent with the results of the MXXLS; moreover, the joint analysis leads to a slope quite close to $\beta = 1/3$. We present all the results in Table 1.

4.1 Comparison with the real data of redMaPPer clusters

We perform a posterior analysis also on the real data from van Uitert & Joachimi (2017): in that work, the clusters contained in the

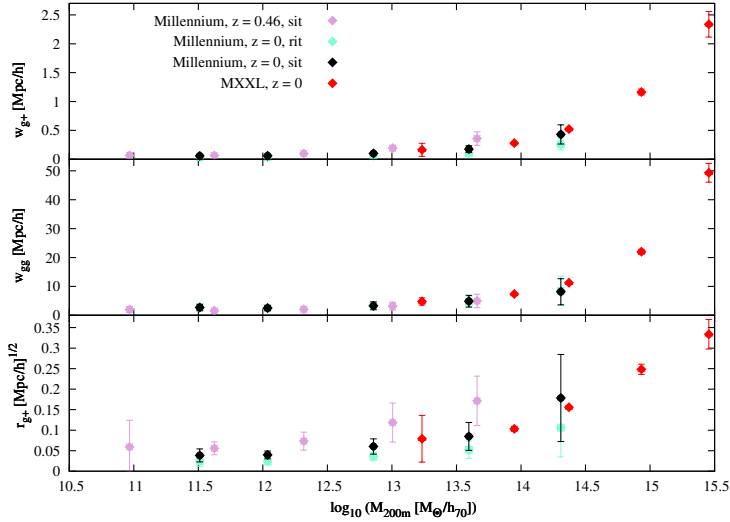


Figure 2. Trend of the intrinsic alignment signal w_{g+} , the cluster signal w_{gg} and r_{g+} as defined in Eq. 16 with the halo mass M_{200m} for the Millennium and the Millennium XXL simulations. The label “sit” stands for “simple inertia tensor”, while “rit” means “reduced inertia tensor”; note that for the MXXLS data only the mass tensor is available, as explained in Sect. 2. As an aside, the purple dots cover a different mass range, namely $10^{11} M_{\odot}$ and $10^{13.5} M_{\odot}$, due to high noise at the high-mass end. The points are not placed at the midpoint of the bin, but at the value corresponding to the arithmetic mean of the mass of the objects.

Table 1. Results of the posterior analysis over the Millennium simulation, the Millennium XXL simulation, their joint contribution and real data. Note the different units of measurement for A in the simulated and real data.

	MS only	MXXLS only	Joint
β	$0.20^{+0.11}_{-0.13}$	$0.35^{+0.03}_{-0.03}$	$0.33^{+0.03}_{-0.03}$
$\log_{10}(A [\text{Mpc}/h]^{1/2})$	$-1.14^{+0.15}_{-0.20}$	$-1.11^{+0.03}_{-0.03}$	$-1.10^{+0.03}_{-0.03}$
Real data			
β	$0.56^{+0.05}_{-0.05}$		
$\log_{10} A$	$0.61^{+0.03}_{-0.04}$		

redMaPPer catalogue (Rykoff et al. 2014) were used to calculate the intrinsic alignment signal amplitude A_{IA} , which was then studied as a function of the halo mass. In van Uitert & Joachimi (2017, figure 7) the results of this analysis are shown together with results from previous works (Joachimi et al. 2011; Singh, Mandelbaum & More 2015): we consider all the 21 points in the plot, neglect the error bars on the mass and treat all the data as independent, so that the covariance matrix is diagonal. In this case, the parameter A is dimensionless, thus making it impossible to directly compare its value to the one that is suggested by the simulation data; moreover, we assume different flat priors in the fit for the parameters, namely $\log_{10} A \in [0.4; 0.9]$ and $\beta \in [0.4; 0.7]$. The outcomes of our analysis are shown in Fig. 4 and in Table 1.

We note that while the disagreement between the values of A can be easily justified, since we are using different definitions of the amplitude of the intrinsic alignment signal, the incompatibility

between the values of the slope β could be explained by a number of more profound factors.

SHALL WE INCLUDE REASONS FOR THE DISCREPANCY?

5 CONCLUSIONS

The last numbered section should briefly summarise what has been done, and describe the final conclusions which the authors draw from their work.

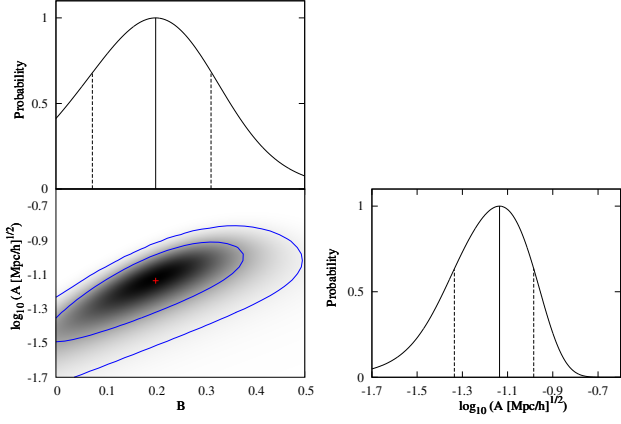
ACKNOWLEDGEMENTS

We thank Mario Bonamigo for providing us with the Millennium XXL catalogue snapshots and Edo van Uitert for making the real data points available to us and for useful discussion about the correct mass units of measurement to use. BJ acknowledges support by an STFC Ernest Rutherford Fellowship, grant reference ST/J004421/1.

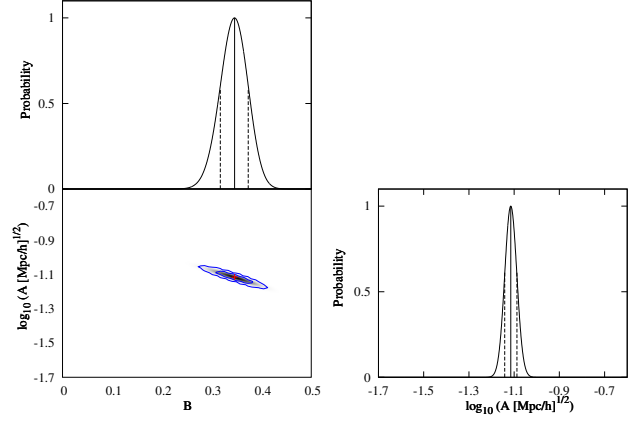
REFERENCES

- Angulo R. E., Springel V., White S. D. M., et al., 2012, *MNRAS*, **426**, 2046
 Bartelmann M., Schneider P., 2001, *Phys. Reports*, **340**, 291
 Bett P., Eke V., Frenk C. S., et al., 2007, *MNRAS*, **376**, 215
 Bonamigo M., Despali G., Limousin M., et al., 2015, *MNRAS*, **449**, 3171
 Chisari N., Codis S., Laigle C., et al., 2015, *MNRAS*, **454**, 2736
 Despali G., Tormen G., Sheth R. K., 2013, *MNRAS*, **431**, 1143
 Joachimi B., Mandelbaum R., Abdalla F. B., Bridle S. L., 2011, *A&A*, **527**, A26
 Joachimi B., Semboloni E., Bett P. E., et al., 2013a, *MNRAS*, **431**, 437
 Joachimi B., Semboloni E., Hilbert S., et al., 2013b, *MNRAS*, **436**, 819
 Joachimi B., Cacciato M., Kitching T. D., et al., 2015, *Space Sci. Rev.*, **193**, 1
 Landy S. D., Szalay A. S., 1993, *ApJ*, **412**, 64
 Pereira M. J., Bryan G. L., Gill S. P. D., 2008, *ApJ*, **672**, 825
 Rykoff E. S., Rozo E., Busha M. T., et al., 2014, *ApJ*, **785**, 104
 Singh S., Mandelbaum R., More S., 2015, *MNRAS*, **450**, 2195
 Springel V., White S. D. M., Jenkins A., et al., 2005, *Nature*, **435**, 629
 Taylor A., Joachimi B., Kitching T., 2013, *MNRAS*, **432**, 1928
 van Uitert E., Joachimi B., 2017, preprint (arXiv:1701.02307v1)

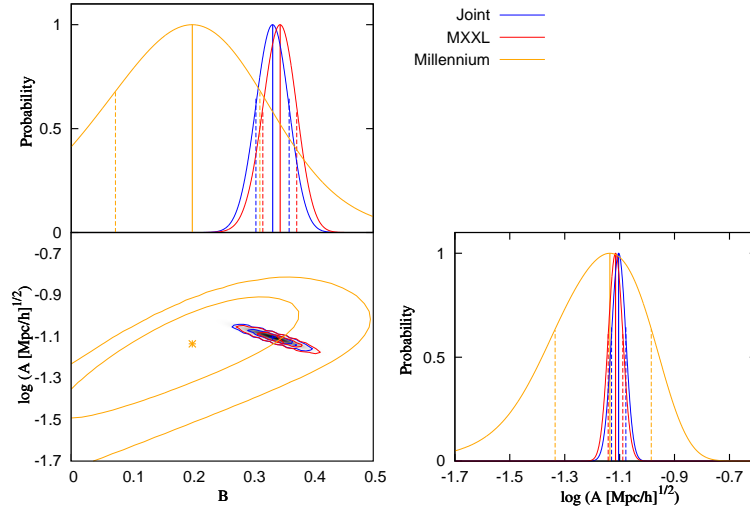
This paper has been typeset from a \LaTeX file prepared by the author.



(a) Posterior analysis for the Millennium simulation.



(b) Posterior analysis for the Millennium XXL simulation.



(c) Joint analysis for both the simulations.

Figure 3. Posterior analysis for (a) the Millennium simulation, (b) the MXXL simulation and (c) joint MS and MXXLS. While the first one returns larger error bars, the results are compatible for the two catalogues; the exact values and errors of A and β are presented in Table 1.

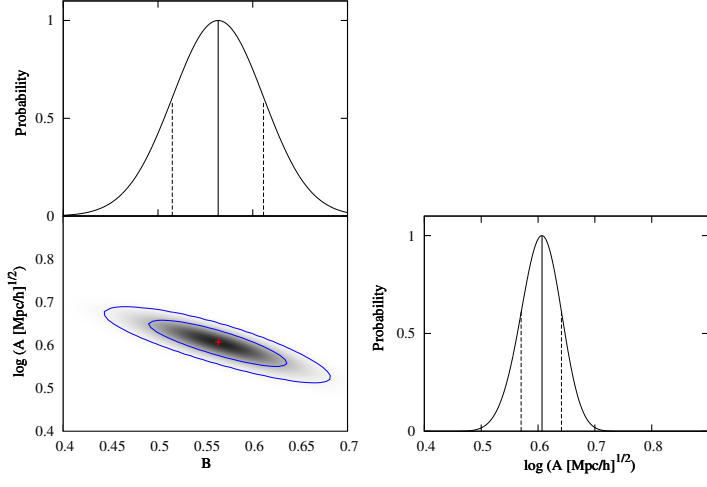


Figure 4. Posterior analysis on the real data; the exact values and errors of A and B are presented in Table 1.